International Journal of Applied Earth Observation and Geoinformation 50 (2016) 117–130

Contents lists available at ScienceDirect

International Journal of Applied Earth Observation and Geoinformation

journal homepage: www.elsevier.com/locate/jag

Mapping tropical forests and deciduous rubber plantations in Hainan Island, China by integrating PALSAR 25-m and multi-temporal Landsat images

Bangqian Chen[a,b], Xiangping Li[a], Xiangming Xiao[a,c,*], Bin Zhao[a], Jinwei Dong[c], Weili Kou[d], Yuanwei Qin[c], Chuan Yang[b], Zhixiang Wu[b], Rui Sun[b], Guoyu Lan[b], Guishui Xie[b]

[a] Institute of Biodiversity Science, Fudan University, No. 2005, Songhu Road, Shanghai 200438, PR China
[b] Rubber Research Institute (RRI), Chinese Academy of Tropical Agricultural Sciences, Danzhou City (CATAS), Danzhou Investigation & Experiment Station of Tropical Cops, Ministry of Agriculture, Hainan Province 571737, PR China
[c] Department of Microbiology and Plant Biology, and Center for Spatial Analysis, University of Oklahoma, Norman, OK 73019, USA
[d] School of Computer Science and Information, Southwest Forestry University, Kunming Yunnan 650224, PR China

ARTICLE INFO

Article history:
Received 10 December 2015
Received in revised form 19 February 2016
Accepted 21 March 2016

Keywords:
Vegetation indices
NDVI
EVI
LSWI
Phenology
Defoliation

ABSTRACT

Updated and accurate maps of tropical forests and industrial plantations, like rubber plantations, are essential for understanding carbon cycle and optimal forest management practices, but existing optical-imagery-based efforts are greatly limited by frequent cloud cover. Here we explored the potential utility of integrating 25-m cloud-free Phased Array type L-band Synthetic Aperture Radar (PALSAR) mosaic product and multi-temporal Landsat images to map forests and rubber plantations in Hainan Island, China. Based on structure information detected by PALSAR and yearly maximum Normalized Difference Vegetation Index (NDVI), we first identified and mapped forests with a producer accuracy (PA) of 96% and user accuracy (UA) of 98%. The resultant forest map showed reasonable spatial and areal agreements with the optical-based forest maps of Fine Resolution Observation and Monitoring Global Land Clover (FROM-GLC) and GlobalLand30. We then extracted rubber plantations from the forest map according to their deciduous features (using minimum Land Surface Water Index, LSWI) and rapid changes in canopies during Rubber Defoliation and Foliation (RDF) period (using standard deviation of LSWI) and dense canopy in growing season (using maximum NDVI). The rubber plantation map yielded a high accuracy when validated by ground truth-based data (PA/UA > 86%) and evaluated with three farm-scale rubber plantation maps (PA/UA >88%). It is estimated that in 2010, Hainan Island had 2.11×10^6 ha of forest and 5.15×10^5 ha of rubber plantations. This study has demonstrated the potential of integrating 25-m PALSAR-based structure information, and Landsat-based spectral and phenology information for mapping tropical forests and rubber plantations.

Published by Elsevier B.V.

1. Introduction

Tropical forests are of vital importance in maintaining biodiversity, sustaining the healthy functioning of ecosystems, and moderating atmospheric greenhouse gas concentration (Lelieveld et al., 2008; Shimada et al., 2014). Considerable amounts of natural forests have been lost due to increasing demands for food and energy (Shimada et al., 2014; Suratman et al., 2004). For example, plantations of rubber (*Hevea brasiliensis* (Wild. ex Adr. de Juss.) Muell Arg.) have expanded rapidly in tropical and subtropical regions in the last 50 years to meet the increasing consumption of natural rubber (Dong et al., 2012b). According to the Food and Agriculture Organization (FAO) of the United Nations Global Forest Resources Assessment (FRA) 2010 report, the global extent of rubber plantations has steadily increased by 25% during the past two decades (FAO, 2010). Although rubber expansion has economically benefited rubber-relevant industries and the owners/producers of rubber plantations, it has also created conflicts between agricultural production and forest management and conservation (de Blecourt et al., 2013; Guardiola-Claramonte et al., 2010; Li et al.,

* Corresponding author.
E-mail addresses: chbq40@163.com (B. Chen), xiangming.xiao@ou.edu (X. Xiao).

http://dx.doi.org/10.1016/j.jag.2016.03.011
0303-2434/Published by Elsevier B.V.

Table 1
Selected recent literatures for mapping forest and deciduous rubber plantations using MODIS/Landsat optical and PALSAR data.

Land cover	Optical data		PALSAR data		PALSAR/Optical data integration/fusion		
	MODIS	Landsat	50-m	25-m	PALSAR 50-m/MODIS	PALSAR 50-m/Landsat	PALSAR 25-m/Landsat
Forest	(Hansen et al., 2003; Razali et al., 2014; Senf et al., 2013)	(Gong et al., 2013; Hansen et al., 2013; Hermosilla et al., 2015)	(Dong et al., 2012a,b, 2014; Longepe et al., 2011; Santoro et al., 2009; Tenku et al., 2015)	(Motohka et al., 2014; Pantze et al., 2014; Shimada et al., 2014; Thapa et al., 2014; Walker et al., 2010)	(Dong et al., 2012a,b; Qin et al., 2015, 2016)	–	(Lehmann et al., 2011, 2012; Reiche et al., 2013, 2015)
Deciduous rubber plantation	(Li and Fox, 2012; Razali et al., 2014; Senf et al., 2013)	(Fan et al., 2015; Li et al., 2015; Li and Fox, 2011a; Suratman et al., 2004)	–	–	(Dong et al., 2012a,b)	(Dong et al., 2013; Kou et al., 2015)	This study

*Only a few optical-based forest mapping literatures were listed here.

2008; Liu et al., 2013; Qiu, 2009; Xu et al., 2014; Ziegler et al., 2009). Accurate and up-to-date maps of natural forests and rubber plantations can provide a better understanding of the consequences of land-cover and land-use change on biodiversity and carbon and water cycles and support decision makers in implementing sustainable management policies. However, a map of rubber plantation extent with high accuracy and spatial resolution is still unavailable in China or Southeast Asia, which currently accounts for approximately 97% of global natural rubber production (FAO, 2010). In addition, the yearly expansion and updating of old rubber plantations also calls for accurate mapping methods to monitor the changes in rubber plantations at local and regional scales.

Satellite remote sensing is a viable approach for large scale forest inventories. Based on the usage of data sources, mapping of forest and deciduous rubber plantations can be classified into three categories: 1) optical image-based approach, 2) Synthetic Aperture Radar (SAR) image-based approach and 3) SAR-optical image integration/fusion approach. The recent literatures from peer-reviewed journals for the most widely used optical and SAR data were summarized in Table 1. Since there are hundreds and thousands of studies employed optical remote sensing for forest mapping because of its early appearance, only a few of them were listed here. The Advanced Very High Resolution Radiometer (AVHRR) (Loveland et al., 2000) and Moderate Resolution Imaging Spectroradiometer (MODIS) (Dong et al., 2012a,b; Hansen et al., 2003; Li and Fox, 2012; Razali et al., 2014; Senf et al., 2013) were the widely used at regional and global scales, but the resultant forest maps often had large uncertainties due to mixtures of land cover types within coarse to moderate resolution imagery pixels. For those medium resolution images such as Landsat Thematic Mapper/Enhanced Thematic Mapper Plus/Operational Land Imager (TM/ETM+/OLI) (Fan et al., 2015; Gong et al., 2013; Hermosilla et al., 2015; Li et al., 2015; Li and Fox, 2011a; Suratman et al., 2005; Zhang et al., 2010), Advance Spaceborne Thermal Emission and Reflectance Radiometer (ASTER) (Li and Fox, 2011b) and SPOT (Mongkolsawat and Putklang, 2010), the major constraints for classification at large scales are the constant presence of clouds and cloud shadows in tropical areas and the long revisit cycles of these sensors (e.g., 16 day revisit for Landsat) (Wang et al., 1999; Watmough et al., 2011; Zhu and Curtis, 2012). Most of these MODIS- and Landsat-based studies have used time series vegetation indices, such as Normalized Difference Vegetation Index (NDVI) (Tucker, 1979), Enhanced Vegetation Index (EVI) (Huete et al., 2002) and Land Surface Water Index (LSWI)(Xiao et al., 2004), which tracks well phenology of vegetation canopy. High spatial resolution images (e.g., IKONOS, Worldview-2) are too expensive for mapping at regional and global scales due to the high image cost (Cho et al., 2015; Mallinis et al., 2008).

SAR data has the advantage of not subjecting to cloud interference, and therefore is a very important complementary data source for land use and land cover study. Long wavelength SAR like Phased Array type L-band SAR (PALSAR) can easily penetrate the forest canopy and capture structural information than short wavelength SAR data (e.g. C-band of ERS (Rosenqvist, 1996) and ENVISAT (Evans and Costa, 2013)). The Japan Earth Resources Satellite (JERS-1, 1992–1998), Advanced Land Observing Satellite (ALOS) PALSAR-1/2 (2006–2010, 2014-present), which are the only satellite-based L-band SAR right now, are widely used for forest mapping and biomass estimation from local to regional scales (Dong et al., 2012a,b, 2014; Liesenberg and Gloaguen, 2013; Longepe et al., 2011; Motohka et al., 2014; Pantze et al., 2014; Peregon and Yamagata, 2013; Shimada et al., 2014; Tenku et al., 2015; Thapa et al., 2014; Walker et al., 2010). In 2011, the Japan Aerospace Exploration Agency (JAXA) released the PALSAR 50-m Orthorectified mosaic image product for the globe to the public. Several studies have assessed the potential of PALSAR 50-m data

for mapping forests in Southeast Asia (Dong et al., 2012a, 2014), China (Qin et al., 2015), and Cameron (Tenku et al., 2015). In 2014, JAXA released PALSAR 25-m Orthorectified mosaic image product for the globe to the public (Shimada et al., 2014). The PALSAR 25-m mosaic product could provide more spatial details about the forest extent and distribution. A few studies have evaluated the potential of PALSAR 25-m data for forest mapping (Motohka et al., 2014; Pantze et al., 2014; Shimada et al., 2014; Thapa et al., 2014), but so far no literatures to evaluate its potential for deciduous rubber plantations mapping.

Integration of both PALSAR and optical data (e.g., MODIS and Landsat) could provide more comprehensive information about vegetation canopy (optical data) and vegetation structure (PALSAR data), which may improve mapping of forests through reducing commission and omission errors. Several studies have evaluated the use of PALSAR 50-m and MODIS data (Dong et al., 2012a,b; Qin et al., 2015) and Landsat data (Dong et al., 2013; Kou et al., 2015) to map forests and deciduous rubber plantations. A couple studies have also evaluated the use of PALSAR 25-m and Landsat data to map forest wetlands such as mangrove forest (Jhonnerie et al., 2015), pine plantations (Jhonnerie et al., 2015), mixed forest (Lehmann et al., 2011, 2012), tropical rain forest (Reiche et al., 2013), and forest growth and degradation stage (Lucas et al., 2014). The objectives of this study is twofold: a) to develop an algorithm that integrates both PALSAR 25-m mosaic data and time-series Landsat images and then apply it to map tropical forests, namely PALSAR/Landsat-based forest and non-forest (F/NF) map; and b) to develop an algorithm that analyzes time-series Landsat images (vegetation indices such as NDVI, EVI and LSWI) and identify and map deciduous rubber plantations in PALSAR/Landsat-based F/NF map. We apply the algorithms to generate maps of forests and deciduous rubber plantations in Hainan Island, the largest rubber production base in China, and evaluate the resultant maps by using ground truth-based data and compare with two optical-image-based F/NF maps of (Fine Resolution Observation and Monitoring-Global Land Cover (FROM-GLC, (Gong et al., 2013; Yu et al., 2013)) and GlobalLand30 (Chen et al., 2015a)). The resultant algorithms and maps of forests and rubber plantations at 30-m spatial resolution are likely to be useful for management of forests and rubber plantations and ecological assessment.

2. Materials and methods

2.1. Study area

Hainan Island (19°20′N ~ 20°10′N, 108°21′E ~ 111°03′E, Fig. 1) is located in the Southern China and has an area of 33,920 km^2. Topography of the island is complex, characterized by hilly regions in the middle surrounded by lowlands in the coastal regions. The Wuzhi Mountain is the highest mountain and has an elevation of 1867-m above sea level. The climate of the island varies from tropical to subtropical. The annual mean temperature is approximately 23–25 °C and monthly temperature varies between ~16 °C in January and to ~30 °C from May to July. The rainy season is May to October. The average annual precipitation is 1500 to 2000 millimeters and can be as high as 2400 millimeters in the central and eastern area and as low as 900 millimeters in the coastal areas of the southwest.

There are a variety of vegetation types on the island. Historically, most of the island was covered by natural forests, but human exploitation led to significant deforestation due to several politico-economic activities such as the Rubber Plantation Campaign in the 1950s and the Land Reclamation Campaigns in the 1960s (Dong et al. 2012b). Natural forest coverage had decreased from 25.7% in 1957 to 9.7% in 1980 (Huang, 2006). After then, extensive reforestation occurred on the island. The statistical estimate of forest area is 2.04 × 10^6 ha in 2011, of which 4.9 × 10^5 ha is rubber plantations (SBHP and SONBSH, 2011). Other managed forests are mainly eucalypt, *acacia mangium*, coconuts, and betel nut.

Table 2
Summary of the Landsat TM/ETM+ images used in this study.

	P123/R046	P124/R046	P123/R047	P124/R047	Total
2008	10/11	10/7	11/5	11/10	42/33
2009	14/5	11/14	16/6	18/13	59/38
2010	5/9	7/7	8/8	6/11	26/35
Total	29/25	28/28	35/19	35/34	127/106

*The first number is TM imagery count, and second number that after backslash is ETM+ images count.

2.2. Satellite imagery and pre-processing

2.2.1. PALSAR dataset and pre-processing

Seven tiles of ALOS PALSAR L-band HH and HV Orthorectified mosaic data (25-m spatial resolution), each covering 1° × 1°, were downloaded from the ALOS Research and Application Project of EORC, JAXA (http://www.eorc.jaxa.jp/ALOS/en/palsar_fnf/data/). This study used 2010 data, mosaicked from raw images acquired between June and August of 2010. The data already have slope correction and radiometric calibration, and are geo-referenced to geographical latitude and longitude coordinates (Shimada et al., 2014). The HH and HV polarization bands were converted from amplitude into normalized radar cross-section backscatter (dB) using Eq. (1) (Rosenqvist et al., 2007):

$$\sigma^0(dB) = 10 \times log_{10}DN^2 + CF \quad (1)$$

where $\sigma^0$is the backscattering coefficient, DN is the digital number value in HH or HV, and CF is the absolute calibration factor set at −83. Two composite images of Ratio (HH/HV) and Difference (HH-HV) were generated as they were widely used for classification (Dong et al., 2012a,b, 2014). PALSAR images and all Landsat images descripted below were re-projected into projection coordinate system of UTM 49N with WGS-84 datum by nearest-neighbor resampling method.

2.2.2. Landsat imagery and pre-processing

Hainan Island is located within four (123/046, 123/047, 124/046 and 124/047) WRS2 path/rows of Landsat images. A total of 233 standard level-one terrain-corrected (L1T) products of Landsat TM/ETM+ imagery from 2008 to 2010 were obtained from the USGS Earth Resources Observation and Science (EROS) Data Center (earthexplorer.usgs.gov) (Table 2).

Landsat image pre-processing includes quality check, atmosphere correction and vegetation indices calculation. Each image was first screened for clouds and their shadows using Fmask software (Zhu and Curtis, 2012) and then converted to surface reflectance using LEDAPS software (Ju et al., 2012; Masek et al., 2013). No gap filling was performed on the ETM+ scan-line-off strips. The vegetation indices of NDVI, EVI and LSWI, which were widely used for mapping forest and rubber plantation (Dong et al., 2012a,b, 2013; Kou et al., 2015; Qin et al., 2016), were calculated using Eqs. (2–4).

$$NDVI = \frac{\rho NIR - \rho red}{\rho NIR + \rho red} \quad (2)$$

$$EVI = 2.5 \times \frac{\rho NIR - \rho red}{\rho NIR^{+6\times} \rho red^{-7.5\times} \rho blue^{+1}} \quad (3)$$

$$LSWI = \frac{\rho NIR - \rho MIR}{\rho NIR + \rho MIR} \quad (4)$$

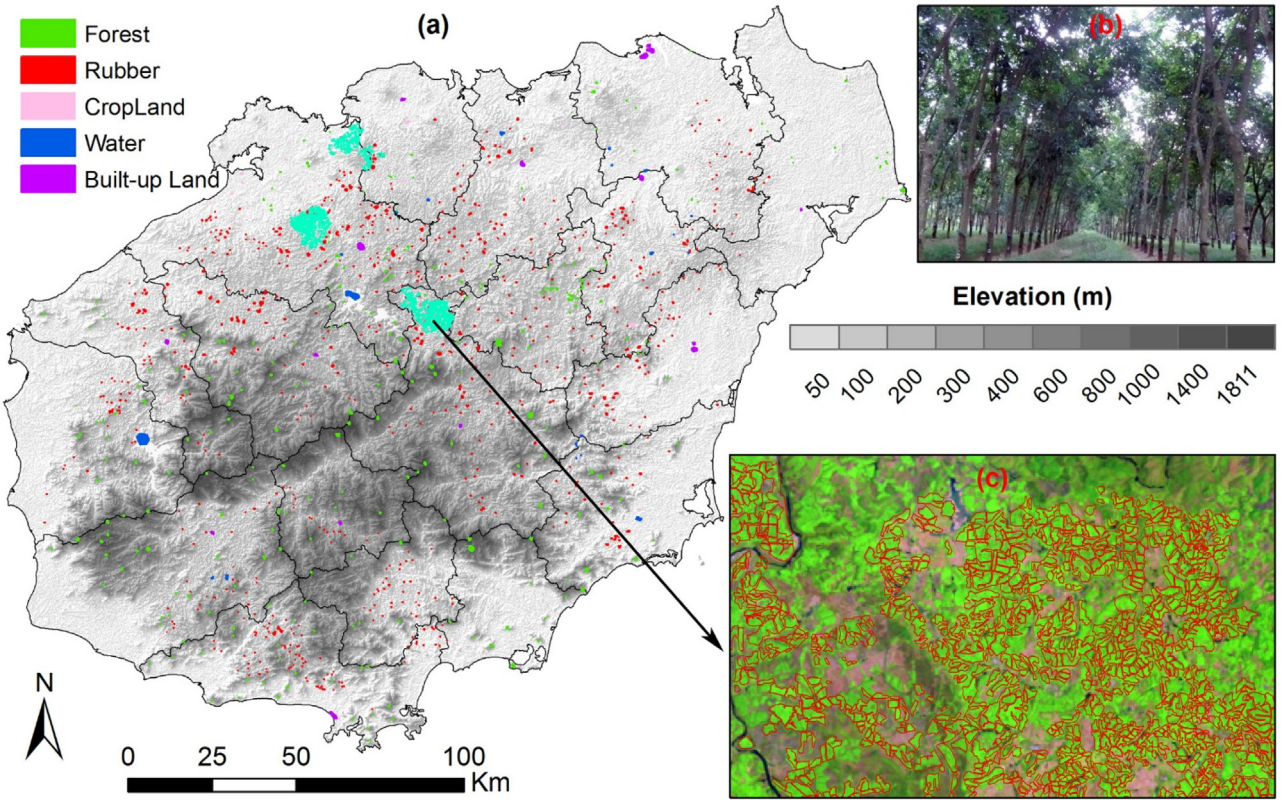

Fig. 1. Topography of Hainan Island and spatial distribution of the ground-truth polygon Region of Interests (ROIs) (a), a photo of rubber plantation taken in 2013 (b), and rubber land-use map of Yangjiang state farm (c) in the study area. The rubber land-use maps were overlapped with Landsat TM imagery acquired on 03/24/2010 and were shown in false color composite (R/G/B = band 5/4/3). The light green color pixels in (c) were rubber plantations. The rubber land-use maps of the Xiqing (top), Yangjiang (middle) and Nanping (bottom) state farm were shown in dense cyan color. (For interpretation of the references to colour in this figure legend, the reader is referred to the web version of this article.)

where $\rho blue$, ρred, ρNIRandρMIR are the surface reflectance of the blue, red, NIR and mid-infrared (MIR) spectral bands, respectively, of Landsat TM/ETM+ imagery.

2.3. Ground reference data

Three field surveys on forests, rubber plantations, and other land cover types were conducted in November 2011, September 2012 and July 2013, respectively. These field photos were taken with a Casio H20G camera embedded with Global Positioning System (GPS) receiver, which records latitude and longitude of the camera, and were uploaded into the Global Geo-Referenced Field Photo Library at the University of Oklahoma (http://www.eomf.ou.edu/photos/, Fig. S1). The library is a free data portal for people to download, upload and share GPS photos. It contains more than 7500 field photos in Hainan Island. Additional field survey data on rubber plantations by other experiments or post-hurricane damage investigations during 2011–2014 were also included in this study. Although the field surveys were carried later than the satellite images acquired in 2008–2010, these photos were still usable because forest and rubber trees usually have a long life span (e.g. rubber trees have economic life span of about 30 years).

The GPS photos and 231 GPS field points of rubber plantations were converted to Google Earth kml files and then loaded into Google Earth. These in-situ data, together with high spatial resolution images taken circa 2010 from Google Earth, were used as reference to delineate Region of Interests (ROIs). We designed systematic sampling grid of 0.5° x 0.5° and tried to draw random polygon ROIs in each grid cells, and finally generated 1118 random distributed polygon ROIs (Fig. 2). Descriptive statistics about the area of the ROIs were presented in Table S1. ROIs for each land use type were randomly divided into training ROIs and validation ROIs at the ratio of 0.3:0.7 by NOAA/NOS/NCCOS/CCMA Biogeography Branch's Design Tool for ArcGIS (http://www2.coastalscience.noaa.gov/publications/detail.aspx?resource=mgAPjEXoVKEOwI+9IXOjBThd9nQ55Og19XX2UqnBEdY=), and their detailed statistics information was shown in Table S2.

2.4. Mapping algorithms

The workflow chart of mapping forest and rubber plantation was presented in Fig. 2. First, we mapped forest using a decision tree method and the 25-m PALSAR data, and the resultant forest map is referred as PALSAR-based F/NF map. Second, we resampled the PALSAR-based F/NF map into 30-m resolution using a nearest neighbor resampling method in ENVI. Third, we generated maximum NDVI (hereinafter referred as $NDVI_{max}$) signatures from time-series Landsat TM/ETM+ images. We overlaid $NDVI_{max}$ data layer with the PALSAR-based F/NF map, and used $NDVI_{max} \geqq 0.65$ to remove the misclassified built-up land from PALSAR-based F/NF map, and the resultant F/NF map was referred as PALSAR/Landsat-based F/NF map. Forth, we discriminated rubber plantation from evergreen forest using $NDVI_{max}$ and signatures of minimum LSWI (hereinafter referred as $LSWI_{min}$) and standard deviation of LSWI (hereinafter referred as $LSWI_{stdev}$) that derived from time-series

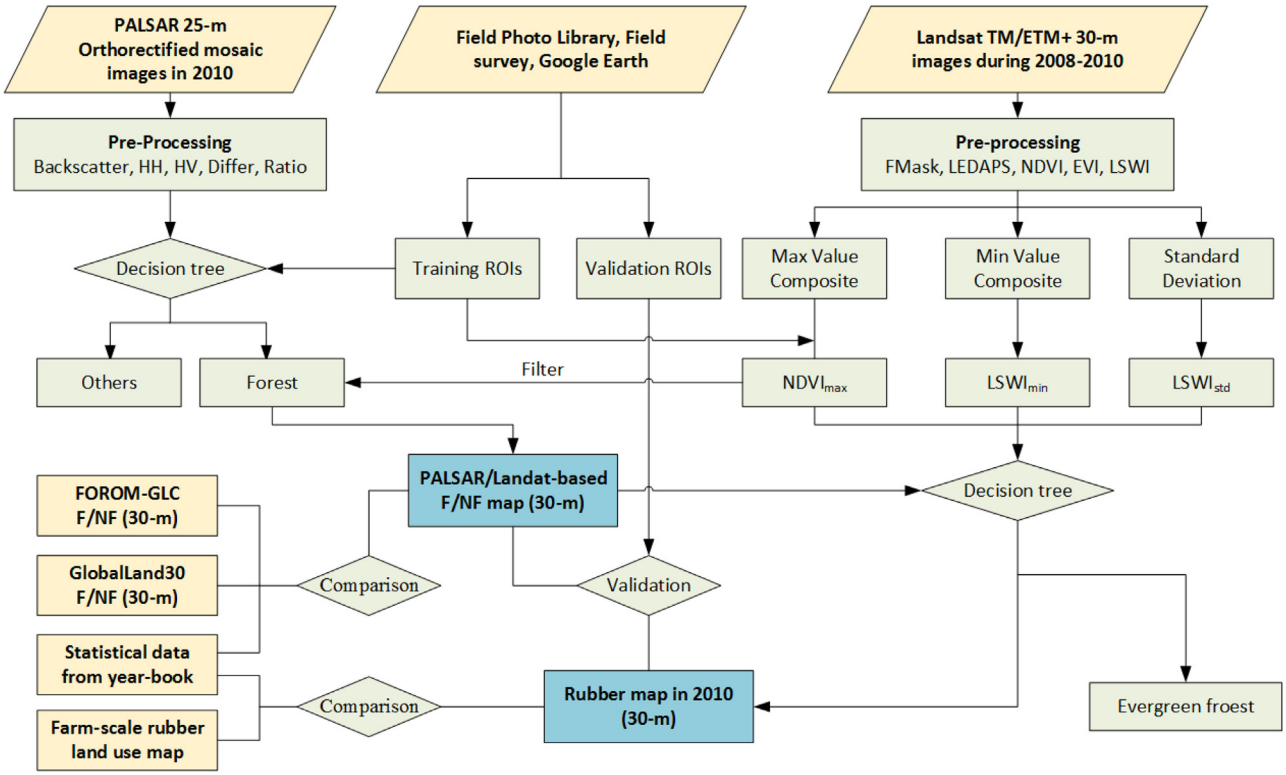

Fig. 2. The workflow of mapping tropical forest and deciduous rubber plantations. (For interpretation of the references to colour in this figure, the reader is referred to the web version of this article.)

optical images acquired during Rubber Defoliation and Foliation (RDF) period of rubber plantation.

2.4.1. *Forest mapping from PALSAR and Landsat images*

According to the FAO, forest is defined as land spanning more than 0.5 ha with tree height of ≧5-m and canopy coverage of ≧10% (FAO, 2010). Forest mapping algorithm was similar to the previous studies reported by Dong et al. (2012a) and Qin et al. (2015), which were performed based on PALSAR 50-m mosaic data. The signature analysis on backscatter values for different land covers were re-performed based on PALSAR 25-m mosaic data with the training ROIs. Frequency distribution histogram of the training ROIs of the forest, cropland, built-up land and water in the bands of HH, HV, Ratio and Difference indicated that water, forest, cropland and built-up land have high separability (Fig. 3). The 95% confidence intervals of the histograms of the individual images (HH, HV, Ratio, and Difference) were used to define thresholds for decision tree rules. The thresholds for HH, HV and Difference were rounded to the 0.5 decimal unit and for the Ratio to 0.05 decimal unit and detailed rules and flows were presented in Fig. 4.

Some buildings or rocks may have similar high backscatter coefficients like forest (Fig. 3b), but they can be separated by NDVI, especially using the highest NDVI value during forest growing season. Maximum value composite with Landsat images acquired during 2009 and 2010 was performed to find the $NDVI_{max}$. The $NDVI_{max}$ histograms for the training ROIs of forest and built-up land and PALSAR-based forest were plotted (Fig. 5). The 5th percentile value of $NDVI_{max}$ for the PALSAR-based forest was used to eliminate those pixels misclassified as forests (0.65 here). We subsequently perform a 3×3 median filter to reduce the salt-and-pepper noise. The image composite processing, and forest and rubber mapping were conducted by the Interactive Data Language (IDL)/ENVI-based programs.

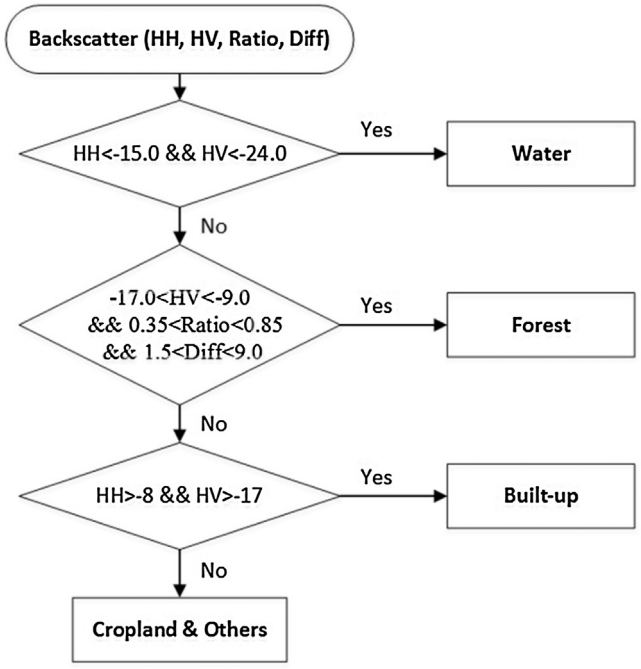

Fig. 4. The decision rules for forest classification based on PALSAR data.

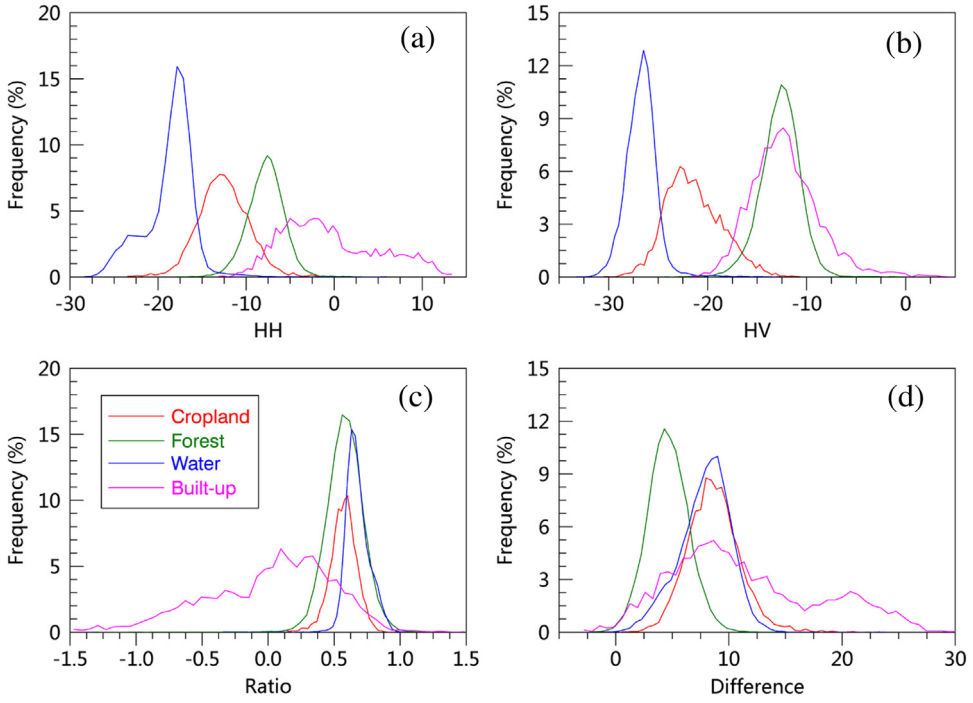

Fig. 3. Frequency histograms of the four land cover types in 25-m PALSAR (a) HH, (b) HV, (c) Ratio (HH/HV), and (d) Difference (HH-HV) band for the training ROIs on Hainan Island, China. (For interpretation of the references to colour in this figure, the reader is referred to the web version of this article.)

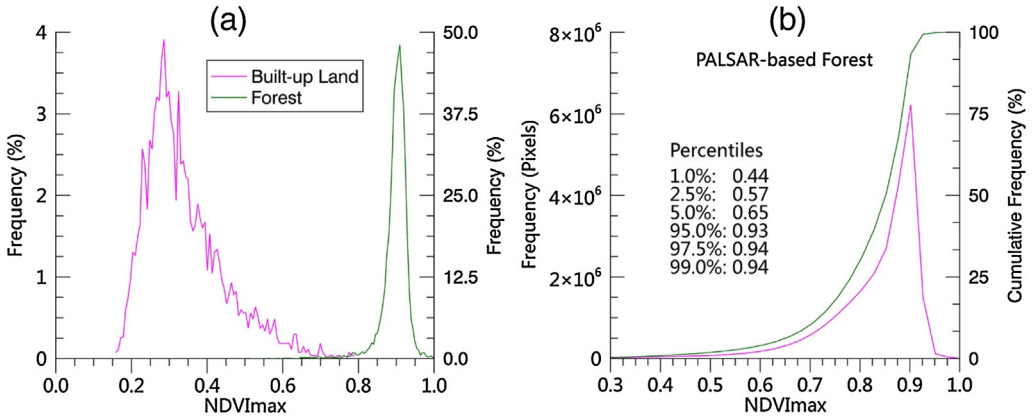

Fig. 5. The $NDVI_{max}$ histogram of training ROIs and PALSAR-based forest pixels: (a) built-up land ROIs against forest ROIs, and (b) PALSAR-based forest pixels. (For interpretation of the references to colour in this figure, the reader is referred to the web version of this article.)

2.4.2. Discriminating deciduous rubber plantation from the forest map

Rubber trees are generally planted 5–8 m apart in rows and 3–4 m in spacing and are under intensive management. They present rapid defoliation (complete or near complete defoliation) and foliation in north tropical area and have dense canopy in growing season. Based on the temporal profiles analysis in our previous studies (Dong et al., 2013; Kou et al., 2015), the minimum value of NIR reflectance and NDVI/EVI/LSWI in RDF period (January to March in Hainan Island) of 2008 and 2010 was used to identify defoliation features. Standard deviation of NIR reflectance and NDVI/EVI/LSWI within RDF period were used to catch the features of rapid changes in canopy. As the RDF period is too short and the cloud coverage is very dense there, images of three consecutive years were used for minimum value composite and computing standard deviation. The $NDVI_{max}$ was selected to identify the feature of dense canopy in growing season, and some secondary forest and managed forests (e.g. Eucalyptus plantation) can be used to eliminated from PALSAR-based forest map if these forest have relative sparse canopy. Finally, good separability between rubber plantations and other forests was found in the $LSWI_{min}$ and $LSWI_{stdev.}$ Histograms of $LSWI_{min}$ and $LSWI_{stdev}$ for training ROIs of rubber plantation and forest, and the histogram and cumulative percentage of $NDVI_{max}$ for the rubber training ROIs were plotted in Fig. 6. The intersection of rubber plantations and forest (Fig. 6a and b, 0.15 and 0.08, respectively) and 5th percentile value of $NDVI_{max}$ (0.85), were used as thresholds. Therefore, the decision rules for separating rubber plantations from PALSAR/Landsat-based F/NF map were $LSWI_{min} < 0.15$ and $LSWI_{stdev} > 0.08$ and $NDVI_{max} > 0.85$.

2.5. Accuracy assessment of forest and rubber plantation maps

The F/NF maps of PALSAR-based, PALSAR/Landsat-based and map of rubber plantation were assessed using a confusion matrix based on the validation ROIs. In addition, three farm-scale rubber plantation vector maps (1: 10,000 scale) were used to evaluate the

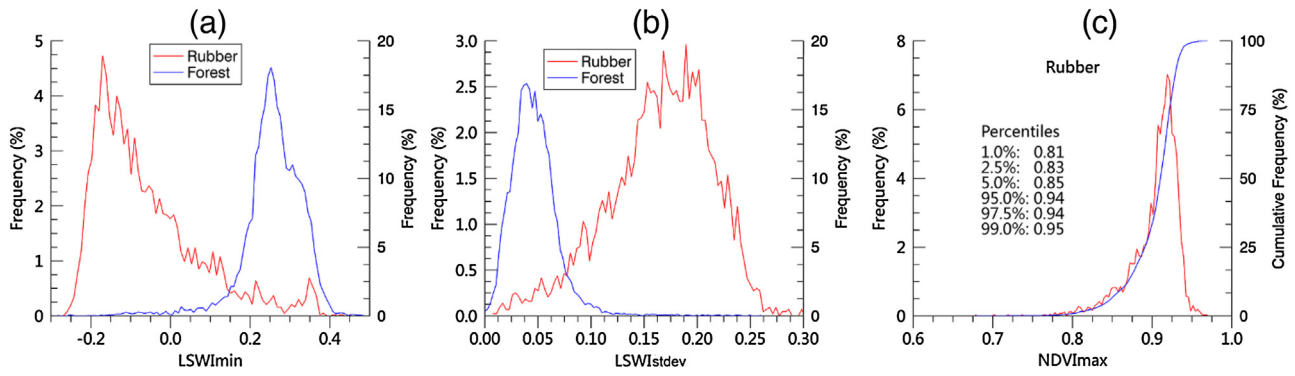

Fig. 6. Frequency histograms of rubber and forest based on training ROIs: (a) $LSWI_{min}$ of deciduous rubber plantations and forests, (b) $LSWI_{stdev}$ of deciduous rubber plantations and forests, and (c) $NDVI_{max}$ and cumulative percentage of deciduous rubber plantations. (For interpretation of the references to colour in this figure, the reader is referred to the web version of this article.)

accuracy of rubber maps. These vector maps were made around 2006 by the Bureau of Hainan State Farms, but polygons of rubber plantations with bare soil background and $NDVI_{max}$ less than 0.85 in the TM/ETM+ images of 2010 were removed in case of land-use change and misclassification. Since the area of rubber plantations at county level did not include state farms, no county level comparison was performed.

2.6. Comparison with available F/NF maps from analyses of Landsat images

The Fine Resolution Observation and Monitoring-Global Land Cover (FROM-GLC) dataset was recently released by researchers in Tsinghua University (http://data.ess.tsinghua.edu.cn, segmentation approach version used here) (Gong et al., 2013; Yu et al., 2013). It was generated from analyses of Landsat TM/ETM+ images in 2010. The GlobalLand30 data was recently released by researchers in the National Geomatics Center of China (NGCC) (www.globallandcover.com) (Chen et al., 2015a). It was generated from analyses of Landsat images and Chinese Environmental and Disaster satellite (HJ-1) images. F/NF maps of Hainan Island were clipped from these two data products at 30-m spatial resolution. The accuracy of the FROM-GLC GlobalLand30 F/NF maps was also assessed using a confusion matrix based on the same ground truth-based ROIs.

We compared our PALSAR/Landsat-based F/NF map with the FROM-GLC and the GlobalLand30 F/NF maps at pixel and county scales. At pixel scale, two forest maps were overlaid with each other to identify those pixels having forests in both maps and those pixels having forests on one map, which shows the agreement between two maps. At county scale, the county boundary map was applied to generate county summary of forest area, using the ENVI/IDL software. Scatterplots and simple linear correlation of forest areas between PALSAR/Landsat-based F/NF map versus FROM-GLC or GlobalLand30 at county scale were used to quantify area agreement between two maps.

3. Results

3.1. F/NF map of Hainan Island in 2010

Spatial distribution of PALSAR-based F/NF map, $NDVI_{max}$, PALSAR/Landsat-based F/NF map is presented in Fig. 7a–c. Good spatial consistency was found between the PALSAR-based F/NF map (Fig. 7a) and the $NDVI_{max}$ (Fig. 7b). Dense forests with high NDVI values are distributed in middle mountain areas. Few forest and low NDVI pixels were located in areas close to the coastline due to intensive human activities. Because buildings have similar high backscatter coefficients as forests in PALSAR HV band, which is a key band in separating forest and cropland and water, a lot of built-up land in urban areas was classified as forests. In Danzhou City (19°31′N, 109°34′E) for example, few forest and low NDVI pixels were found in the urban area (Fig. 8a and b), but there remained a large number of buildings misclassified as forest pixels (Fig. 9c). After filtering the pixels with $NDVI_{max}$ less than 0.65 (5th percentile of PALSAR-based forest pixels), most misclassified pixels in the city and coastline were removed (Figs. 8d and 7c).

Table 3
Accuracy assessment of different F/NF maps in 2010 in Hainan Island using ground truth-based ROIs.

F/NF products	PA (%)	UA (%)	OA (%)	KC
PALSAR/Landsat-based	96.3	98.4	96.8	0.93
FROM-GLC	82.0	95.8	86.9	0.73
GlobalLand30	91.3	90.9	89.2	0.77

*PA: producer's accuracy, UA: user's accuracy, OA: overall accuracy, KC: kappa coefficient.

3.2. Comparison between PALSAR/Landsat-based and optical-image based F/NF maps in 2010

Accuracy assessments of these three F/NF maps with ground truth-based ROIs are presented in Table 3. A total of 647 ground-truth forest ROIs (34,675 pixels, equal to 3121 ha) and 136 non-forest ROIs (22,165 pixels, equal to 1995 ha) were used for validation (Table S2). User's accuracy (UA), producer's accuracy (PA), overall accuracy (OA) and kappa coefficient (KC) for the PALSAR/Landsat-based F/NF map is 98.4%, 96.3%, 96.8%, and 0.93, respectively. Among these F/NF maps, the PALSAR/Landsat-based map shows the highest overall accuracy, then followed by GlobalLand30 (OA = 89.2%) and FROM-GLC (OA = 86.9%), respectively.

At the pixel scale, the forests of PALSAR/Landsat-based F/NF map shows similar spatial distribution with the forest of FORM-GLC and GlobalLand30 F/NF map in most regions (Fig. 1a–c), particularly in the mountain regions (Fig. 1). The difference map between PALSAR/Landsat F/NF map and the FROM-GLC F/NF map (Fig. 9d) has 17,955,632 pixels in agreement, accounting for 76.4% of the PALSAR/Landsat F/NF map, and 81.0% of the FROM-GLC F/NF map. The difference map between the PALSAR/Landsat N/NF map and the GlobalLand30 F/NF map (Fig. 9e) has 19,782,933 pixels in agreement, account of 84.2% of the PALSAR/Landsat F/NF map, and 73.9% of the Globaland30 F/NF map.

At the county scale, forest area of the 18 counties from PALSAR/Landsat-based F/NF map is high correlated with the results from FROM-GLC ($R^2 = 0.81$) and GlobalLand30 ($R^2 = 0.80$) (Fig. 9f). The fitted lines are close to one-to-one line. However, about four counties obviously have few forest areas in FROM-GLC F/NF map

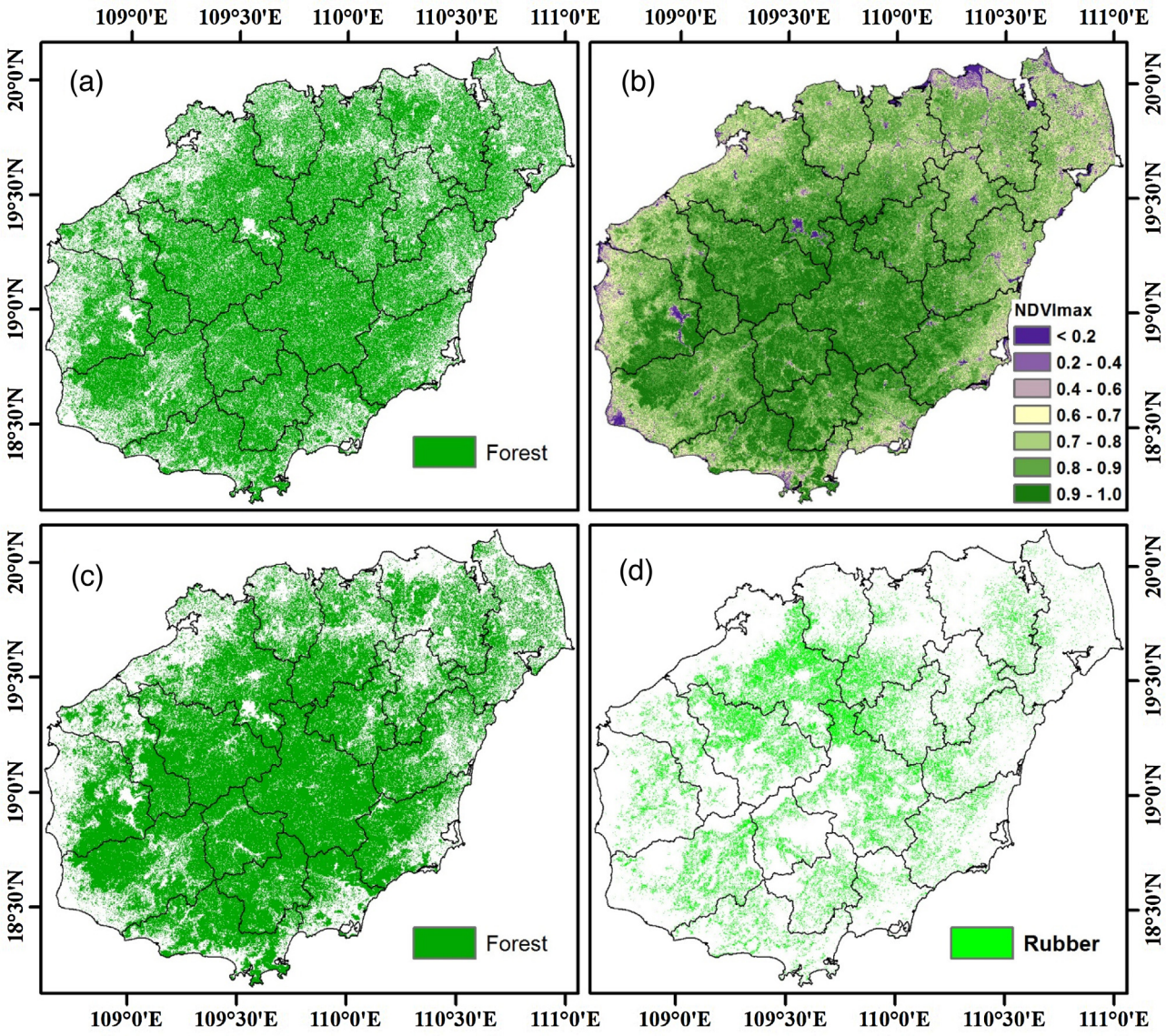

Fig. 7. Spatial distribution of (a) PALSAR-based F/NF map, (b) maximum value composite NDVI ($NDVI_{max}$), (c) PALSAR/Landsat-based F/NF map, and (d) deciduous rubber plantation map in Hainan Island in 2010. (For interpretation of the references to colour in this figure, the reader is referred to the web version of this article.)

than the results from PALSAR/Landsat-based F/NF map. More than half of the counties has more forest in GlobalLand30 F/NF map than the results from PALSAR/Landsat-based F/NF map.

The total forest area in Hainan Island from the F/NF map of PALSAR/Landsat-based, FROM-GLC and GlobalLand30 are 2.11×10^6 ha, 2.00×10^6 ha and 2.41×10^6 ha, respectively. The total forest area from PALSAR/Landsat-based and FROM-GLC F/NF maps are quite consistent with the value of 2.04×10^6 ha that reported in the 2011 statistical yearbook (SBHP and SONBSH, 2011). Since the PALSAR/Landsat-based F/NF shows reasonable spatial distribution of forest and holds the highest accuracy when validated with ground truth-based ROIs, it can serve as a reliable base map for rubber plantation mapping.

3.3. Map of deciduous rubber plantations on Hainan Island in 2010

The rubber plantation map is presented in Fig. 8d. Rubber plantations are mainly distributed in the northern central area, follow by the western and southern areas. The densest rubber plantation area is located in Danzhou City and its surrounding regions, which comprise the largest natural rubber production base on Hainan Island.

Accuracy assessment of the rubber plantation map is first using 452 ground-truth rubber ROIs (11,216 pixels, equal to 1009 ha) and 331 non-rubber ROIs (45,614 pixels, equal to 4105 ha) and the results is presented in Table 4. The UA, PA, OA and KC for rubber plantations were 89.4%, 86.1%, 95.2% and 0.85, respectively. The total number of rubber pixels on the Hainan Island in 2010 is 5,723,453, equal to 5.15×10^5 ha, which is about 5% higher than the 2011 statistical yearbook's value (4.9×10^5 ha).

The resultant map also corresponds well with vector maps of rubber plantations from three state-run plantation farms (location shown in Fig. 1a). Except for a few regions to the north of Xiqing (19.559N, 109.450E) and Nanping (18.58N, 109.91E) state farms, the disagreement pixels are distributed randomly on these farms (Fig. 10). The agreement pixel account for 94.3%, 88.1% and 96.2% of the state farms in Xiqing, Nanping, and Yangjiang (19.297N, 109.758E), respectively. The higher accuracies of Xiqing and Yangjiang state farms compared to the Nanping state farms may be explained by the limitation of the satellite images. The Nanping state farm is located in the southeast region of the Hainan

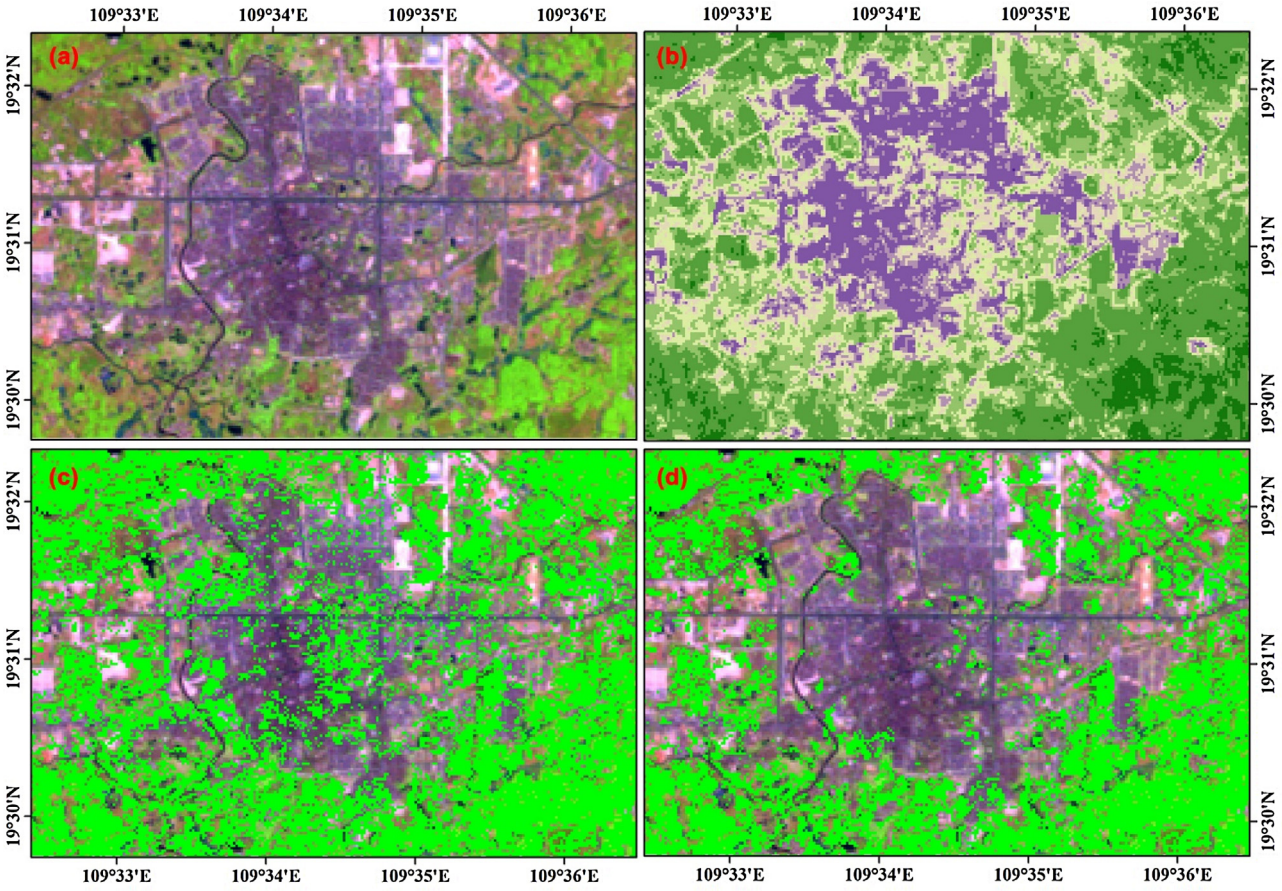

Fig. 8. Schematic diagram of improving forest mapping accuracy with $NDVI_{max}$ filtration in Danzhou City, Hainan Island, China: (a) False color composite of Landsat TM imagery on 03/24/2010 (R/G/B = Band 5/4/3), (b) Spatial distribution of $NDVI_{max}$, (c) Overlapped PALSAR-based F/NF map with TM imagery, and (d) Overlapped PALSAR/Landsat-based F/NF map with TM imagery after $NDVI_{max} \geqq 0.65$ filtration. The legend in (b) is the same as in Fig. 7b. (For interpretation of the references to colour in this figure, the reader is referred to the web version of this article.)

Table 4
Accuracy assessment of deciduous rubber plantation map in Hainan Island, China.

		User (Ground truth pixels)		Total map pixels	User's accuracy (%)
	Class	Rubber	Non-rubber		
Producer (map pixels)	Rubber	9652	1143	10795	89.4
	Non-rubber	1564	44471	46035	96.6
Total ground truth pixels		11216	45614	56830	
Producer's accuracy (%)		86.1	97.5		

*The overall accuracy is 95.2% and kappa coefficients is 0.85. Non-rubber category includes ROIs of forest, cropland, water and built-up lands.

Island, where few cloud-free images were available due to high precipitation and clouds there.

4. Discussion

4.1. Algorithms for mapping forests with PALSAR 25-m and Landsat data

PALSAR L-band has been proved as an effective data source for forest mapping (Dong et al., 2012a,b, 2014; Shimada et al., 2014; Thapa et al., 2014). The signatures of forest, cropland, water and built-up land on the PALSAR 25 -m mosaic product have similar patterns with the results of the PALSAR 50-m mosaic product in Mainland Southeast Asia (Dong et al., 2012a,b) and China (Qin et al., 2015), but differ slightly in boundary values. Forests have higher HH and HV values due to their large crown canopies that depolarize incident radiation, and their threshold intervals were slightly larger than the results based on the 50-m products. These thresholds need to be evaluated before applied to other regions, as a recent study shows varying thresholds for global-scale forest mapping (Shimada et al., 2014).

Built-up land, however, have HV and HH values overlapped with forests to some degree because of complex environments such as building orientations and corner reflectance. The NDVI from the maximum value composite image was very effective in getting rid of misclassified forest pixels in urban areas by creating a threshold (e.g. 0.65 used here). Qin et al. (2015) has resampled 250-m MODIS NDVI to 50-m resolution to mask out built-up lands, barren lands and sparsely vegetated lands with complex structure and rough land surface, therefore improved the accuracy of forest map that derived PALSAR 50-m data. The maximum NDVI from Landsat data, however, would provide more spatial details than the MODIS

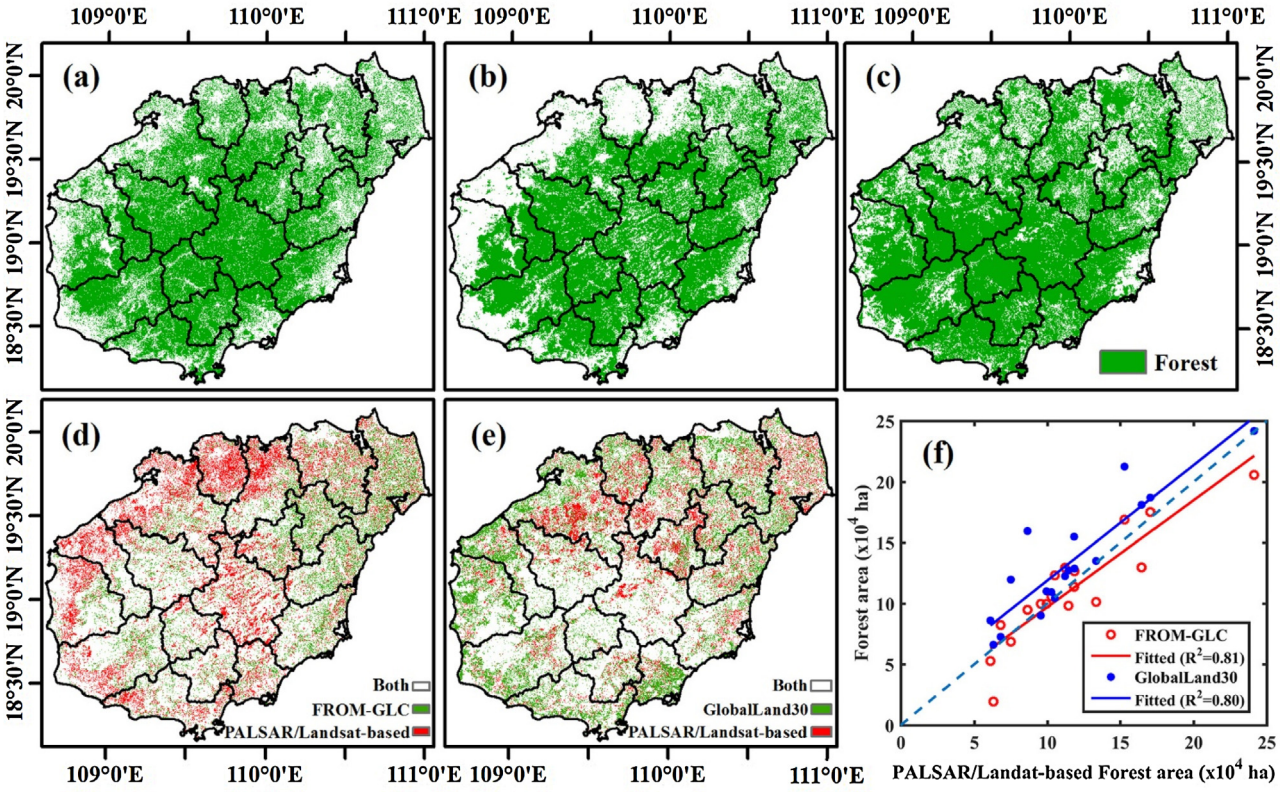

Fig. 9. Comparison between PALSAR/Landsat-based and optical-based F/NF maps of Hainan Island in 2010: (a) PALSAR/Landsat-based F/NF map, (b) FROM-GLC F/NF map, (c) GlobalLand30 F/NF map, (d) Difference forest map between F/NF maps of PALSAR/Landsat-based and FROM-GLC, (e) Difference forest map between F/NF maps of PALSAR/Landsat-based and GlobalLand30, (f) Scatter and regression plot of forest area from F/NF maps of PALSAR/Landsat-based against FROM-GLC and GlobalLand30 at county scale. (For interpretation of the references to colour in this figure, the reader is referred to the web version of this article.)

NDVI. In addition, several previous studies have also demonstrated the potential of mapping forests by integrating PALSAR and optical imagery. For example, the Landsat-derived foliage projective cover (FPC), which was estimated from multiple regression relationships between field measurements and Landsat sensor bands, was used to map forest growth and degradation stages with PALSAR 25-m mosaic data (Lucas et al., 2014); Reiche et al. (2015) proposed a pixel-based Multi-sensor Time-series correlation and Fusion approach (MulTiFuse) to fuse Landsat NDVI and PALSAR L-band backscatter time series to detect deforestation; Lehmann et al. (2015) investigated the level of discrimination between forest and non-forest by using the canonical variate analysis with Landsat data, RADASAT-2 and PALSAR data. Compared with these studies, filtration with NDVI that derived from time series TM/ETM+ seems to be more straightforward at a fine resolution and easier to automate at both regional and global scales.

The PALSAR/Landsat-based F/NF map showed reasonable areal and spatial agreement with the 30-m scale optical-image based F/NF maps of FROM-GLC and GlobalLand30 in most regions (Fig. 9). The improved accuracy of PALSAR/Landsat-based F/NF map (PA/UA > 96%) over FROM-GLC (PA/UA > 87) and GlobalLand30 (PA/UA > 89%) benefits from the incorporation of both optical and SAR data. The differences between these F/NF maps may be explained by the result of the definition of forest, the data sources, and the algorithms (Qin et al., 2015). For example, the F/NF map of FROM-GLC was generated from Random Forest (RF) classifier (Yu et al., 2013), and the GlobalLand30 was derived from pixel- and object-based methods with a knowledge (POK-Based) approach with minimum mapping unit of 8 × 8 30-m pixels for forest (Chen et al., 2015a).

4.2. Algorithm for mapping deciduous rubber plantation

Several studies have indicated that optical-image based signatures (e.g. surface reflectance and vegetation indices) during RDF period are key information for discriminating deciduous rubber plantations from forest landscape (Dong et al., 2012a,b, 2013; Fan et al., 2015; Kou et al., 2015; Li et al., 2015), and phenology-based algorithms are more prevalent recently since they can generate more accurate map. Dong et al. (2012b) explored the temporal profiles of rubber plantations based on 250-m MOD13Q1 product, and then used mean NDVI in RDF period (January–March) and May to July to discriminate rubber plantations from 50-m PALSAR-based forest map in Hainan Island, China. MODIS data have high temporal resolution to track phenology change in rubber plantations but limits its suitability due to its coarse spatial resolution (250–500 m) and fragmented landscapes in tropics. Subsequently, Dong et al. (2013) investigated the temporal profile of rubber plantation based on time-series Landsat data and indicated that rubber plantations can be delineated within forest map using one to two images acquired in RDF period, and a 30-m resolution map of rubber plantations in Danzhou City, Hainan Island, China was obtained. Recently, rubber plantation maps of Xishuangbanna, Yunan Province, China almost simultaneous generated using change rate of Normalized Difference Ratio (NBR) (Li et al., 2015) and difference of NDVI/EVI/ARVI (Atmospherically Resistant Vegetation Index)/NDMI (Normalized Difference Moisture Index)/TCG (Tasseled Cap Greenness) (Fan et al., 2015) from bi-temporal cloud-free Landsat OLI images, which were acquired in RDF period. Single and bi-temporal images based algorithms are limited at regional scale and for a given time since they rely on cloud-free images

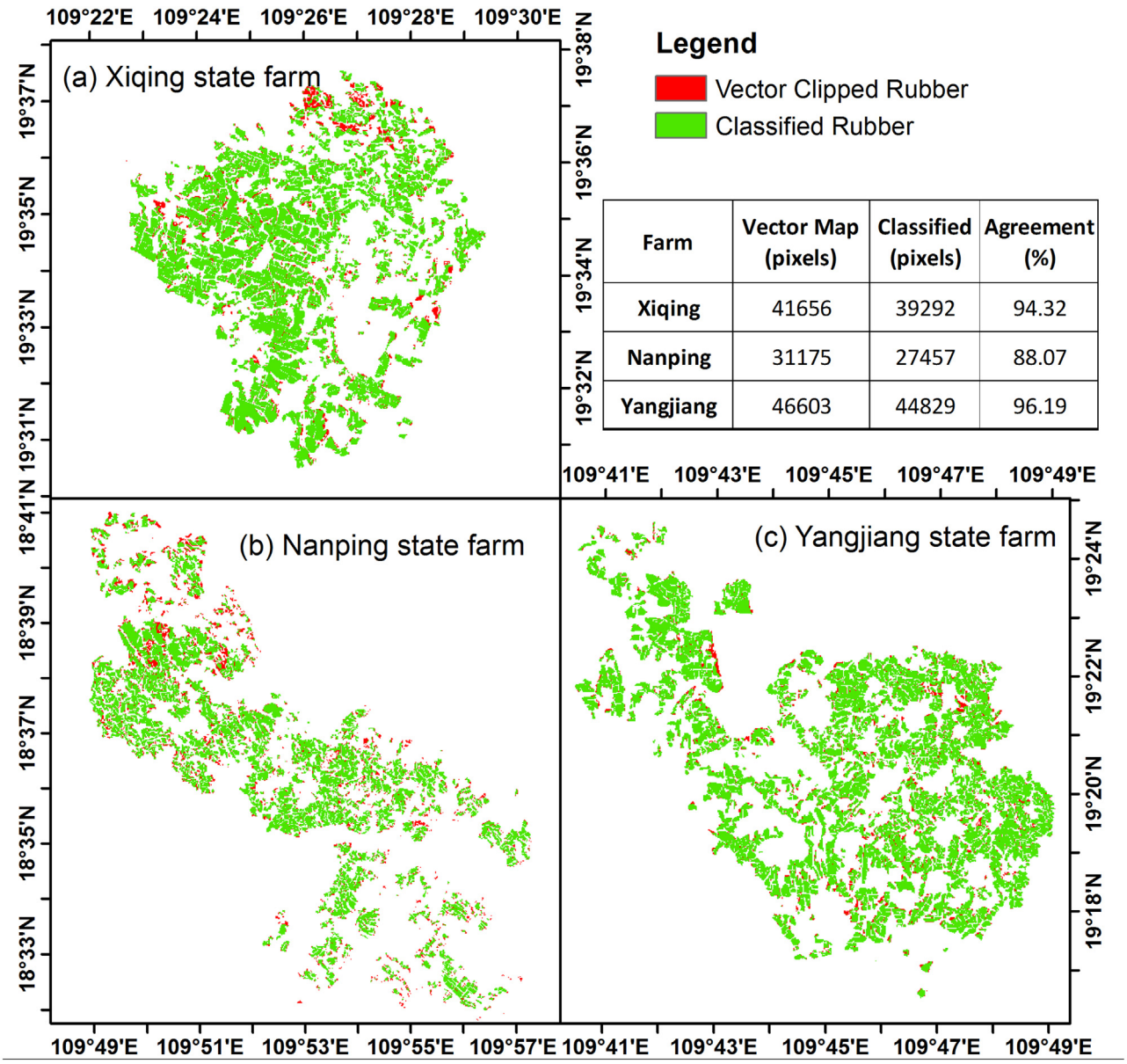

Farm	Vector Map (pixels)	Classified (pixels)	Agreement (%)
Xiqing	41656	39292	94.32
Nanping	31175	27457	88.07
Yangjiang	46603	44829	96.19

Fig. 10. Agreement between classified rubber plantations and vector clipped rubber plantations in: (a) Xiqing farm in Danzhou City, (b) Yangjiang farm in Qiongzhong City, and (c) Nanping farm in Lingshui City. The classified rubber maps are showed in green color and their background were raster maps converted from rubber vector maps. The disagreement between these two maps is shown in red and the pixel size in table is 30-m. (For interpretation of the references to colour in this figure legend, the reader is referred to the web version of this article.)

acquired in RDF period, which is very short and always accompany with dense cloud cover in tropical areas. Therefore, compromise during mapping deciduous rubber plantations should be reached by compositing images acquired in RDF period and from multiple years. Kou et al. (2015) proposed using minimum value of LSWI and NDVI composited from one year's Landsat TM/ETM+ images acquired in RDF period to overcome the problem of clouds and mapped rubber plantation in Xishuangbanna, Yunnan province, China. The minimum values of NIR/NDVI/EVI/LSWI during RDF period are more practical as decision rules when considering inter-annual phenology differences. For example, complete defoliation in rubber plantations was observed about one month earlier in 2014 than 2013 in experimental farm of Chinese Academy of Tropical Agricultural Sciences (CATAS) (Chen et al., 2015b). In addition, the phenology difference at different latitudes can be minimized using signatures from minimum value composite images over a large area (e.g., the climate of Hainan Island varies from tropical to subtropical).

Signatures from single, bi-temporal images and minimum values of composited images are good indicator to identify deciduous rubber plantations, but commission and omission errors can be further eliminated if incorporated more features of rubber plantations for mapping. For example, change rate of NBR for some croplands may also very high when it used as decision rules, and some non-rubber deciduous forest would be classified as rubber plantations if only relay on minimum LSWI/EVI/NDVI as thresholds. In the tropics do exist non-rubber deciduous forests, especially in the mountains where have arid climate (Fig. 11a and b). Here we proposed integrating three most important features to identify rubber plantations from forest landscape: 1) complete or near complete defoliation features, 2) rapid changes of canopy during RDF period and 3) dense canopy in growing season. Complete or near complete defoliation features have been explored by previous

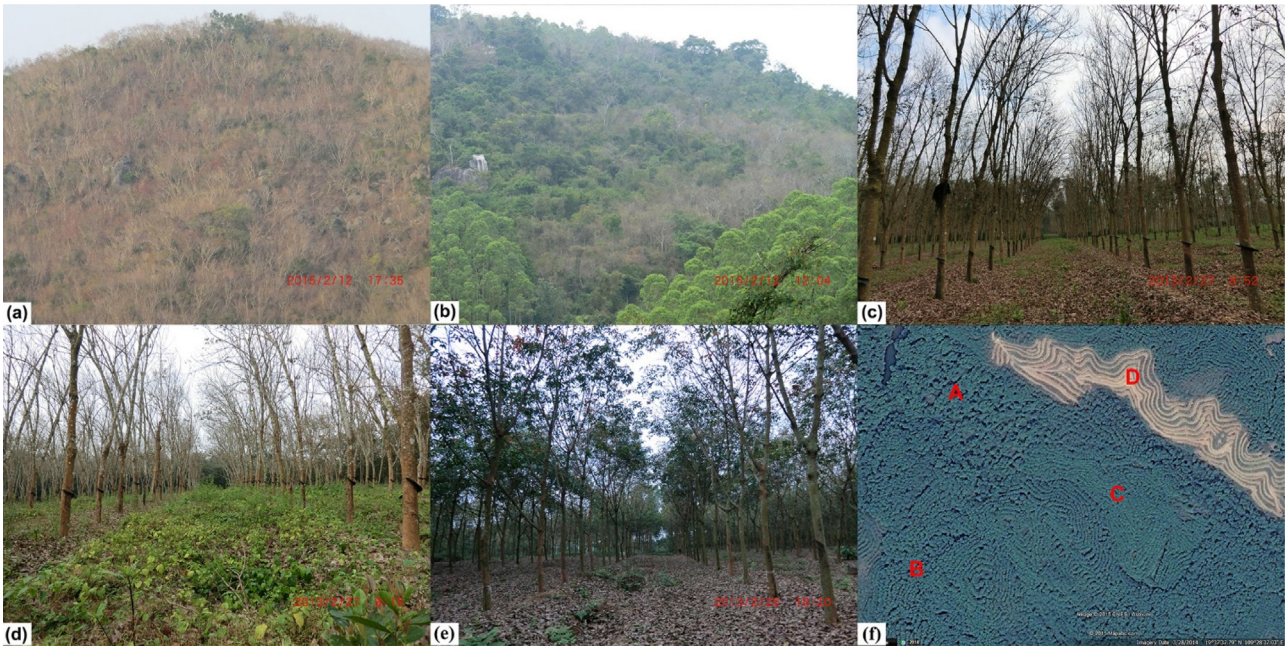

Fig. 11. Field photos illustrating classification uncertainty for mapping rubber plantations: (a) non-rubber deciduous forest (18.3679°N, 109.9923°E) observed in February near Sanya City, Hainan Island, (b) mixed evergreen and non-rubber deciduous forest (18.9407°N, 109.9394°E) in Ledong City, Hainan Island, (c) plantation with completely defoliation and clear understory, (d) plantation with completely defoliation but dense understory, (e) plantation with most leaves on tree during the defoliation stage, and (f) stand gaps created by hurricanes, viewed from Google earth (19.6298°N, 109.4757°E). (For interpretation of the references to colour in this figure, the reader is referred to the web version of this article.)

studies and minimum value of surface reflectance or vegetation indices from time series optical images are good indicators to mark it (Kou et al., 2015). Our field measurement of LAI from 30 rubber plantations in CATAS experimental farm during 2012–2014 showed the rapid change of canopy during RDF period, of which the mean LAI quickly dropped from 3.35 m^2/m^2 in January to 0.91 m^2/m^2 in February and increased to 3.89 m^2/m^2 in March (Chen et al., 2015b). The rapid variation in canopy is more likely been recorded by multiple satellite images and it is reasonable that deciduous rubber plantations clearly hold a higher $LSWI_{stdev}$ than that of the evergreen forest, which undergoes limited seasonal water stress and keeps foliage year round. In addition, deciduous rubber plantations are under intensive management, such as regular fertilization (Chen et al., 2011), and will possess high LAI values in growing season. The largest mean LAI in CATAS experimental farm can reach $5.27 \pm 0.79\ m^2/m^2$ in later September 2013 (Chen et al., 2015b). High LAI will contribute to high NDVI value, and sparse forests that unlikely to be rubber plantations can be removed using NDVI ($NDVI_{max} > 0.85$ used here). Though the NDVI threshold may seem a little large (Gamon et al., 1995), it is reasonable as it was calculated based on surface reflectance data. Previous study found that surface reflectance-based NDVI is clearly larger than the NDVI based on digital number, radiance or top of atmosphere reflectance data (Soudani et al., 2006).

4.3. Uncertainty analysis

Understory vegetation and unsynchronized phenology of rubber plantations were the two important factors that affect the classification accuracy. The richness of understory vegetation was related to water environment and management measures. For example, the understory vegetation was cut down regularly for green manure, killed by herbicides, and grazed by livestock. Besides, the frequent typhoons on the island have resulted in a large number of gaps in the middle-aged and aged plantations and, consequently, accelerated the growth of understory vegetation (Chen et al., 2012). In addition, quick development of understory vegetation is usually accompanied by defoliation due to the opening of the canopy. The unsynchronized phenology of some rubber plantations was closely related to the site-specific environment, clones, stand age, and improper fertilization methods and time (He and Huang, 1987). The quick development of understory vegetation and unsynchronized phenology in rubber plantations would increase the LSWI value, and make it more difficult to separate them from evergreen forest. Fig. 11 **(c-e)** illustrates the typical state of the canopy and understory vegetation of the rubber plantations during the RDF period. Fig. 11**c** was an ideal rubber plantation for classification because the sparse understory vegetation and complete defoliation would lead to a negative LSWI ($LSWI_{min} < 0$). $LSWI_{min}$ may be close to zero for Fig. 11**d** and above zero for Fig. 11**e**. The stand age of rubber plantations in Fig. 11**f** was A>B>C, and D was newly updating plantation. The old plantation (**Fig f A**) obviously had large gaps and dense understory due to the frequent hurricane disturbances. The phenological-based algorithm can identify plantations like Fig. 11**c** and probably includes plantations as Fig. 11**d**, but may fail to discriminate plantations similar to Fig. 11**e** and Fig. 11**f A**.

Although additional deciduous signatures of rubber plantations can be detected if more Landsat TM/ETM+ images were used for compositing, a compromise should be reached between the image timespan and land-use change. An image timespan of two to three years is recommended for mapping rubber plantations over large area. In addition, rubber plantations less than four years old were mostly seedlings and have open canopy, therefore cannot be classified as forest. The total discrepancy (about 15%) between the PALSAR/Landsat-based rubber plantation map and the statistical data may be explained in part by uncertainty in classification and statistics. For example, privately owned rubber plantations increased dramatically since 2000 and had accounted for more than half of the total rubber plantations on the island in 2009 (Mo,

2010). Unlike the state-owned plantations, these private plantations scarcely have detailed planting records and are difficult to be precise statistics.

5. Conclusions

Understanding the area and spatial distribution of tropical forests and rubber plantations are of vital importance for ecological studying and sustainable management. As a follow-up to our previous studies (Dong et al., 2013; Kou et al., 2015; Qin et al., 2015), here we have investigated the potential of PALSAR 25-m mosaic data for forest mapping, and incorporated maximum value composite NDVI from time-series Landsat images to improve mapping accuracy. The resultant F/NF map from this algorithm showed very high accuracy (PA/UA > 96%) and reasonable spatial and areal agreements with the optical-image based forest maps of FROM-GLC and GlobalLand30. In addition, we proposed an integration of deciduous features (using $LSWI_{min}$) and rapid changes in canopies in RDF period (using $LSWI_{stdev}$) and dense canopy in growing season (using $NDVI_{max}$) to discriminate deciduous rubber plantations from PALSAR-based forest map. The application of the algorithm demonstrated great potential with high accuracy maps of rubber plantation (PA/UA > 86%) in Hainan Island, China. Further studies may focus on extending and validating the algorithm and workflow to address tropical forest dynamics and deciduous rubber plantations at a larger spatial extent (e.g. South China and the Southeast Asia) and longer time span (2007–2010 and 2015-) with historical PALSAR and Landsat data as well as upcoming data source such as PALSAR-2 and Sentinel-2.

Acknowledgments

This research was funded in part by the Earmarked Fund for China Agriculture Research System (CARS-34-GW5), National Natural Science Foundation of China (41571408, 31400493), US NASA Land Use and Land Cover Change program (NNX11AJ35G). The Fundamental Research Funds for Rubber Research Institute, CATAS (1630022015012). We thank the U.S Geological Survey (USGS) EROS Data Center and JAXA for their image products and thank Drs. Xueyang and Yadong Zhou in Hainan Forestry Department, Drs. Qinghuo Lin, Hailiang Li and Zhongliang Tao in CATAS for providing part of the field data or vector maps. We also thank Sarah Xiao at Yale University for English language editing of the manuscript.

Appendix A. Supplementary data

Supplementary data associated with this article can be found, in the online version, at http://dx.doi.org/10.1016/j.jag.2016.03.011.

References

Chen, B., Cao, J., Wang, J., Wu, Z., Xie, G., 2011. Development and implementation of site-Specific fertilizer recommendation model based on nutrient balance for rubber plantation. Agron. J. 103, 464–471.

Chen, B., Cao, J., Wang, J., Wu, Z., Tao, Z., Chen, J., Yang, C., Xie, G., 2012. Estimation of rubber stand age in typhoon and chilling injury afflicted area with Landsat TM data A case study in Hainan Island, China. For. Ecol. Manage. 274, 222–230.

Chen, B., Wu, Z., Yang, C., Qi, D., Li, X., Lan, G., Xie, G., Tao, Z., Shun, R., Xiao, X., 2015b. Monthly dynamic of leaf area index of rubber plantation in Danzhou, Hainan Island, China. Chin. J. Trop. Agric. 35, 1–7.

Chen, J., Chen, J., Liao, A., Cao, X., Chen, L., Chen, X., He, C., Han, G., Peng, S., Lu, M., Zhang, W., Tong, X., Mills, J., 2015a. Global land cover mapping at 30m resolution: a POK-based operational approach. ISPRS J. Photogramm. Remote Sens. 103, 7–27.

Cho, M.A., Malahlela, O., Ramoelo, A., 2015. Assessing the utility WorldView-2 imagery for tree species mapping in South African subtropical humid forest and the conservation implications: dukuduku forest patch as case study. Int. J. Appl. Earth Obs. Geoinf. 38, 349–357.

de Blecourt, M., Brumme, R., Xu, J., Corre, M.D., Veldkamp, E., 2013. Soil carbon stocks decrease following conversion of secondary forests to rubber (Hevea brasiliensis) plantations. PLoS One. 8, e69357.

Dong, J., Xiao, X., Sheldon, S., Biradar, C., Duong, N.D., Hazarika, M., 2012a. A comparison of forest cover maps in Mainland Southeast Asia from multiple sources: pALSAR, MERIS, MODIS and FRA. Remote Sens. Environ., 60–73.

Dong, J., Xiao, X., Sheldon, S., Biradar, C., Xie, G., 2012b. Mapping tropical forests and rubber plantations in complex landscapes by integrating PALSAR and MODIS imagery. ISPRS J. Photogramm. Remote Sens. 74, 20–33.

Dong, J., Xiao, X., Chen, B., Torbick, N., Jin, C., Zhang, G., Biradar, C., 2013. Mapping deciduous rubber plantations through integration of PALSAR and multi-temporal Landsat imagery. Remote Sens. Environ. 134, 392–402.

Dong, J., Xiao, X., Sheldon, S., Biradar, C., Zhang, G., Duong, N.D., Hazarika, M., Wikantika, K., Takeuhci, W., Moore, B.R., 2014. A 50-m forest cover map in Southeast Asia from ALOS/PALSAR and its application on forest fragmentation assessment. PLoS One. 9, e85801.

Evans, T.L., Costa, M., 2013. Landcover classification of the lower nhecolândia subregion of the brazilian pantanal wetlands using ALOS/PALSAR, RADARSAT-2 and ENVISAT/ASAR imagery. Remote Sens. Environ. 128, 118–137.

FAO, 2010. Global Forest Resources Assessment 2010. Food and Agriculture Organization of the United Nations (FAO).

Fan, H., Fu, X., Zhang, Z., Wu, Q., 2015. Phenology-based vegetation index differencing for mapping of rubber plantations using landsat OLI data. Remote Sens. 7, 6041–6058.

Gamon, J.A., Field, C.B., Goulden, M.L., Griffin, K.L., Hartley, A.E., Joel, G., Peñuelas, J., Valentini, R., 1995. Relationships between NDVI, canopy structrue, and photosynthesis in three californian vegetation types. Ecol. Appl. 5, 28–41.

Gong, P., Wang, J., Yu, L., Zhao, Y., Zhao, Y., Liang, L., Niu, Z., Huang, X., Fu, H., Liu, S., Li, C., Li, X., Fu, W., Liu, C., Xu, Y., Wang, X., Cheng, Q., Hu, L., Yao, W., Zhang, H., Zhu, P., Zhao, Z., Zhang, H., Zheng, Y., Ji, L., Zhang, Y., Chen, H., Yan, A., Guo, J., Yu, L., Wang, L., Liu, X., Shi, T., Zhu, M., Chen, Y., Yang, G., Tang, P., Xu, B., Giri, C., Clinton, N., Zhu, Z., Chen, J., Chen, J., 2013. Finer resolution observation and monitoring of global land cover: first mapping results with Landsat TM and ETM+ data. Int. J. Remote Sens. 34, 2607–2654.

Guardiola-Claramonte, M., Troch, P.A., Ziegler, A.D., Giambelluca, T.W., Durcik, M., Vogler, J.B., Nullet, M.A., 2010. Hydrologic effects of the expansion of rubber (Hevea brasiliensis) in a tropical catchment. Ecohydrology 3, 306–314.

Hansen, M.C., DeFries, R.S., Townshend, J.R.G., Carroll, M., Dimiceli, C., Sohlberg, R.A., 2003. Global percent tree cover at a spatial resolution of 500 meters: first results of the MODIS vegetation continuous fields algorithm. Earth Interact. 7, 1–15.

Hansen, M.C., Potapov, P.V., Moore, R., Hancher, M., Turubanova, S.A., Tyukavina, A., Thau, D., Stehman, S.V., Goetz, S.J., Loveland, T.R., Kommareddy, A., Egorov, A., Chini, L., Justice, C.O., Townshend, J.R.G., 2013. High-resolution global maps of 21st-century forest cover change. Science 342, 850–853.

He, K., Huang, Z., 1987. Rubber Culture in the Northern Part of Tropical Area. Guangdong Science & Technology Press, Guangdong.

Hermosilla, T., Wulder, M.A., White, J.C., Coops, N.C., Hobart, G.W., 2015. Regional detection, characterization, and attribution of annual forest change from 1984 to 2012 using Landsat-derived time-series metrics. Remote Sens. Environ. 170, 121–132.

Huang, J., 2006. Study on Sustainable Management of Tropical Forest in Hainan Island, China. Chinese Academy of Forestry, Beijing.

Huete, A., Didan, K., Miura, T., Rodriguez, E.P., Gao, X., Ferreira, L.G., 2002. Overview of the radiometric and biophysical performance of the MODIS vegetation indices. Remote Sens. Environ. 83, 195–213.

Jhonnerie, R., Siregar, V.P., Nababan, B., Prasetyo, L.B., Wouthuyzen, S., 2015. Random forest classification for mangrove land cover mapping using landsat 5 TM and alos PALSAR imageries. Procedia Environ. Sci. 24, 215–221.

Ju, J., Roy, D.P., Vermote, E., Masek, J., Kovalskyy, V., 2012. Continental-scale validation of MODIS-based and LEDAPS Landsat ETM+ atmospheric correction methods. Remote Sens. Environ. 122, 175–184.

Kou, W., Xiao, X., Dong, J., Gan, S., Zhai, D., Zhang, G., Qin, Y., Li, L., 2015. Mapping deciduous rubber plantation areas and stand ages with PALSAR and landsat images. Remote Sens. 7, 1048–1073.

Lehmann, E., Caccetta, P., Zhou, Z.S., Mitchell, A., Tapley, I., Milne, A., Held, A., Lowell, K., McNeill, S., 2011. Forest discrimination analysis of combined Landsat and ALOS-PALSAR data. Proceeding of International Symposium for Remote Sensing of the Environment.

Lehmann, E.A., Caccetta, P.A., Zhou, Z., McNeill, S.J., Wu, X., Mitchell, A.L., 2012. Joint processing of landsat and ALOS-PALSAR data for forest mapping and monitoring. IEEE Trans. Geosci. Remote Sens. 50, 55–67.

Lehmann, E.A., Caccetta, P., Lowell, K., Mitchell, A., Zhou, Z., Held, A., Milne, T., Tapley, I., 2015. SAR and optical remote sensing: assessment of complementarity and interoperability in the context of a large-scale operational forest monitoring system. Remote Sens. Environ. 156, 335–348.

Lelieveld, J., Butler, T.M., Crowley, J.N., Dillon, T.J., Fischer, H., Ganzeveld, L., Harder, H., Lawrence, M.G., Martinez, M., Taraborrelli, D., Williams, J., 2008. Atmospheric oxidation capacity sustained by a tropical forest. Nature 452, 737–740.

Li, Z., Fox, J.M., 2011a. Rubber tree distribution mapping in northeast Thailand. Int. J. Geosci. 02, 573–584.

Li, Z., Fox, J.M., 2011b. Integrating Mahalanobis typicalities with a neural network for rubber distribution mapping. Remote Sens. Lett. 2, 157–166.

Li, Z., Fox, J.M., 2012. Mapping rubber tree growth in mainland Southeast Asia using time-series MODIS 250m NDVI and statistical data. Appl. Geogr. 32, 420–432.

Li, H., Ma, Y., Aide, T.M., Liu, W., 2008. Past, present and future land-use in Xishuangbanna: China and the implications for carbon dynamics. For. Ecol. Manage. 255, 16–24.
Li, P., Zhang, J., Feng, Z., 2015. Mapping rubber tree plantations using a Landsat-based phenological algorithm in Xishuangbanna, southwest China. Remote Sens. Lett. 6, 49–58.
Liesenberg, V., Gloaguen, R., 2013. Evaluating SAR polarization modes at L-band for forest classification purposes in Eastern Amazon, Brazil. Int. J. Appl. Earth Obs. Geoinf. 21, 122–135.
Liu, H., Blagodatskiy, S., Cadisch, G., 2013. Soil and Carbon Loss within Watersheds Affected by Rubber Cultivation in Xishuangbanna, South-West China. Tropentag, Stuttgart-Hohenheim, Germany.
Longepe, N., Rakwatin, P., Isoguchi, O., Shimada, M., Uryu, Y., Yulianto, K., 2011. Assessment of ALOS PALSAR 50m orthorectified FBD data for regional land cover classification by support vector machines. IEEE Trans. Geosci. Remote Sens. 49, 2135–2150.
Loveland, T.R., Reed, B.C., Brown, J.F., Ohlen, D.O., Zhu, Z., Yang, L., Merchant, J.W., 2000. Development of a global land cover characteristics database and IGBP DISCover from 1km AVHRR data. Int. J. Remote Sens. 21, 1303–1330.
Lucas, R.M., Clewley, D., Accad, A., Butler, D., Armston, J., Bowen, M., Bunting, P., Carreiras, J., Dwyer, J., Eyre, T., Kelly, A., McAlpine, C., Pollock, S., Seabrook, L., 2014. Mapping forest growth and degradation stage in the Brigalow Belt Bioregion of Australia through integration of ALOS PALSAR and Landsat-derived foliage projective cover data. Remote Sens. Environ. 155, 42–57.
Mallinis, G., Koutsias, N., Tsakiri-Strati, M., Karteris, M., 2008. Object-based classification using Quickbird imagery for delineating forest vegetation polygons in a Mediterranean test site. ISPRS J. Photogramm. Remote Sens. 63, 237–250.
Masek, J.G., Vermote, E.F., Saleous, N., Wolfe, R., Hall, F.G., Huemmrich, F., Gao, F., Kutler, J., Lim., T.K., 2013. LEDAPS Calibration, Reflectance, Atmospheric Correction Preprocessing Code, Version 2. In.
Mo, Y., 2010. Production and marketing of nature rubber in 2009 and market forecast in 2010. China Trop. Agric., 12–15.
Mongkolsawat, W., Putklang, C., 2010. An approach for estimating area of rubber plantation: integrating satellite and physical data over the northeast Thailand. Proceedings of the 31th Asian Conference on Remote Sensing Vietnam.
Motohka, T., Shimada, M., Uryu, Y., Setiabudi, B., 2014. Using time series PALSAR gamma nought mosaics for automatic detection of tropical deforestation A test study in Riau, Indonesia. Remote Sens. Environ. 155, 79–88.
Pantze, A., Santoro, M., Fransson, J.E.S., 2014. Change detection of boreal forest using bi-temporal ALOS PALSAR backscatter data. Remote Sens. Environ. 155, 120–128.
Peregon, A., Yamagata, Y., 2013. The use of ALOS/PALSAR backscatter to estimate above-ground forest biomass: a case study in Western Siberia. Remote Sens. Environ. 137, 139–146.
Qin, Y., Xiao, X., Dong, J., Zhang, G., Shimada, M., Liu, J., Li, C., Kou, W., Moore, B., 2015. Forest cover maps of China in 2010 from multiple approaches and data sources PALSAR, Landsat, MODIS, FRA, and NFI. ISPRS J. Photogramm. Remote Sens. 109, 1–16.
Qin, Y., Xiao, X., Dong, J., Zhang, G., Roy, P.S., Joshi, P.K., Gilani, H., Murthy, M.S.R., Jin, C., Wang, J., Zhang, Y., Chen, B., Menarguez, M.A., Biradar, C.M., Bajgain, R., Li, X., Dai, S., Hou, Y., Xin, F., Moore III, B., 2016. Mapping forests in monsoon Asia with ALOS PALSAR 50-m mosaic images and MODIS imagery in 2010. 6, 20880.
Qiu, J., 2009. Where the rubber meets the garden. Nature 457, 246–247.
Razali, S., Marin, A., Nuruddin, A., Shafri, H., Hamid, H., 2014. Capability of integrated MODIS imagery and ALOS for oil palm: rubber and forest areas mapping in tropical forest regions. Sensors 14, 8259–8282.
Reiche, J., Souzax, C.M., Hoekman, D.H., Verbesselt, J., Persaud, H., Herold, M., 2013. Feature level fusion of multi-Temporal ALOS PALSAR and landsat data for mapping and monitoring of tropical deforestation and forest degradation. IEEE J. Sel. Top. Appl. Earth Obs. Remote Sens. 6, 2159–2173.
Reiche, J., Verbesselt, J., Hoekman, D., Herold, M., 2015. Fusing Landsat and SAR time series to detect deforestation in the tropics. Remote Sens. Environ. 156, 276–293.
Rosenqvist, A., Shimada, M., Ito, N., Watanabe, M., 2007. ALOS PALSAR: a pathfinder mission for global-scale monitoring of the environment. IEEE Trans. Geosci. Remote Sens. 11, 3307–3316.
Rosenqvist, Å., 1996. Evaluation of JERS-1, ERS-1 and Almaz SAR backscatter for rubber and oil palm stands in West Malaysia. Int. J. Remote Sens. 17, 3219–3231.
SBHP, SONBSH, 2011. Hainan Statistical Yearbook 2011. China Statistics Press.
Santoro, M., Fransson, J.E.S., Eriksson, L.E.B., Magnusson, M., Ulander, L.M.H., Olsson, H., 2009. Signatures of ALOS PALSAR L-Band backscatter in swedish forest. IEEE Trans. Geosci. Remote Sens. 47, 4001–4019.
Senf, C., Pflugmacher, D., van der Linden, S., Hostert, P., 2013. Mapping rubber plantations and natural forests in xishuangbanna (Southwest China) using multi-Spectral phenological metrics from MODIS time series. Remote Sens. 5, 2795–2812.
Shimada, M., Itoh, T., Motooka, T., Watanabe, M., Shiraishi, T., Thapa, R., Lucas, R., 2014. New global forest/non-forest maps from ALOS PALSAR data (2007–2010). Remote Sens. Environ. 155, 13–31.
Soudani, K., François, C., le Maire, G., Le Dantec, V., Dufrêne, E., 2006. Comparative analysis of IKONOS, SPOT, and ETM+ data for leaf area index estimation in temperate coniferous and deciduous forest stands. Remote Sens. Environ. 102, 161–175.
Suratman, M.N., Bull, G.Q., Leckie, D.G., Lemay, V.M., Marshall, P.L., Mispan, M.R., 2004. Prediction models for estimating the area, volume, and age of rubber (Hevea brasiliensis) plantations in Malaysia using Landsat TM data. Int. For. Rev. 6, 1–12.
Suratman, N.M., LeMay, V.M., Bull, G.Q., Leckie, D.G., Walsworth, N., Marshall, P.L., 2005. Logistic regression modeling of thematic mapper data for rubber (Hevea brasiliensis) area mapping. Sci. Lett. 2, 79–84.
Tenku, S.N., Xiao, X., Dong, J., 2015. Depicting forest cover in Grand South of Cameroon: an analysis based on L-band PALSAR 50-m orthorectified imagery. Afr. J. Wood Sci. For. 3, 198–210.
Thapa, R.B., Itoh, T., Shimada, M., Watanabe, M., Takeshi, M., Shiraishi, T., 2014. Evaluation of ALOS PALSAR sensitivity for characterizing natural forest cover in wider tropical areas. Remote Sens. Environ. 155, 32–41.
Tucker, C.J., 1979. Red and photographic infrared linear combinations for monitoring vegetation. Remote Sens. Environ. 8, 127–150.
Walker, W.S., Stickler, C.M., Kellndorfer, J.M., Kirsch, K.M., Nepstad, D.C., 2010. Large-Area classification and mapping of forest and land cover in the brazilian amazon: a comparative analysis of ALOS/PALSAR and landsat data sources. IEEE J. Sel. Top. Appl. Earth Obs. Remote Sens. 3, 594–604.
Wang, B., Ono, A., Muramatsu, K., Fujiwara, N., 1999. Automated detection and removal of clouds and their shadows from Landsat TM images. IEICE Trans. Inf. Syst. E82, 453–460.
Watmough, G.R., Atkinson, P.M., Hutton, C.W., 2011. A combined spectral and object-based approach to transparent cloud removal in an operational setting for Landsat ETM+. Int. J. Appl. Earth Obs. Geoinf. 13, 220–227.
Xiao, X., Hollinger, D., Aber, J., Goltz, M., Davidson, E.A., Zhang, Q., Moore, B., 2004. Satellite-based modeling of gross primary production in an evergreen needleleaf forest. Remote Sens. Environ. 89, 519–534.
Xu, J., Grumbine, R.E., Becksch Fer, P., 2014. Landscape transformation through the use of ecological and socioeconomic indicators in Xishuangbanna Southwest China Mekong Region. Ecol. Indic. 36, 749–756.
Yu, L., Wang, J., Gong, P., 2013. Improving 30 meter global land cover map FROM-GLC with time series MODIS and auxiliary datasets: a segmentation based approach. Int. J. Remote Sens. 34, 5851–5867.
Zhang, J., Tao, Z., Liu, S., Cai, D., Tian, G., Xie, R., Xu, X., 2010. Rubber planting acreage calculation in hainan island based on TM image. Chin. J. Trop. Crops 31, 661–665.
Zhu, Z., Curtis, W., 2012. Object-based cloud and cloud shadow detection in Landsat imagery. Remote Sens. Environ. 118, 83–94.
Ziegler, A.D., Fox, J.M., Xu, J., 2009. The rubber juggernaut. Science 324, 1024–1025.

Supplementary Online Materials

Table S1. Descriptive statistics of the area of the polygon ROIs

	No. ROIs	Area (ha)				
		Mean	Median	Std.Dev	Min	Max
Forest	278	11.93	5.95	17.78	0.4	152.04
Rubber	646	2.1	1.58	1.87	0.11	18.06
Cropland	109	8.52	3.05	17.06	0.2	143.75
Built-up	43	15.32	4.74	24.23	0.44	104.94
Water	42	50.96	15.53	143.59	0.17	815.31

*. Forest and rubber ROIs were regarded as forest ROIs during forest mapping phase, while built-up land, water and cropland ROIs were used as non-forest ROIs. When validating the results of rubber plantation, forest, built-up land, water and cropland ROIs were regard as non-rubber ROIs.

Table S2. The polygon ROIs used for mapping forests and rubber plantations.

	Forest	Rubber	Cropland	Built-up land	Water
Training ROIs	83(13227)	194(4585)	32(4711)	13(2682)	13(12170)
Validation ROIs	195(23459)	452(11216)	77(5764)	30(4673)	29(11728)

*. The first values are ROI number, and the second in bracket are corresponding pixel number in 30-m Landsat TM/ETM+ imagery. Forest and rubber ROIs were regarded as forest ROIs during forest mapping phase, while built-up land, water and cropland ROIs were used as non-forest ROIs. When validate the results of rubber plantation, forest, built-up land, water and cropland ROIs were regard as non-rubber ROIs.

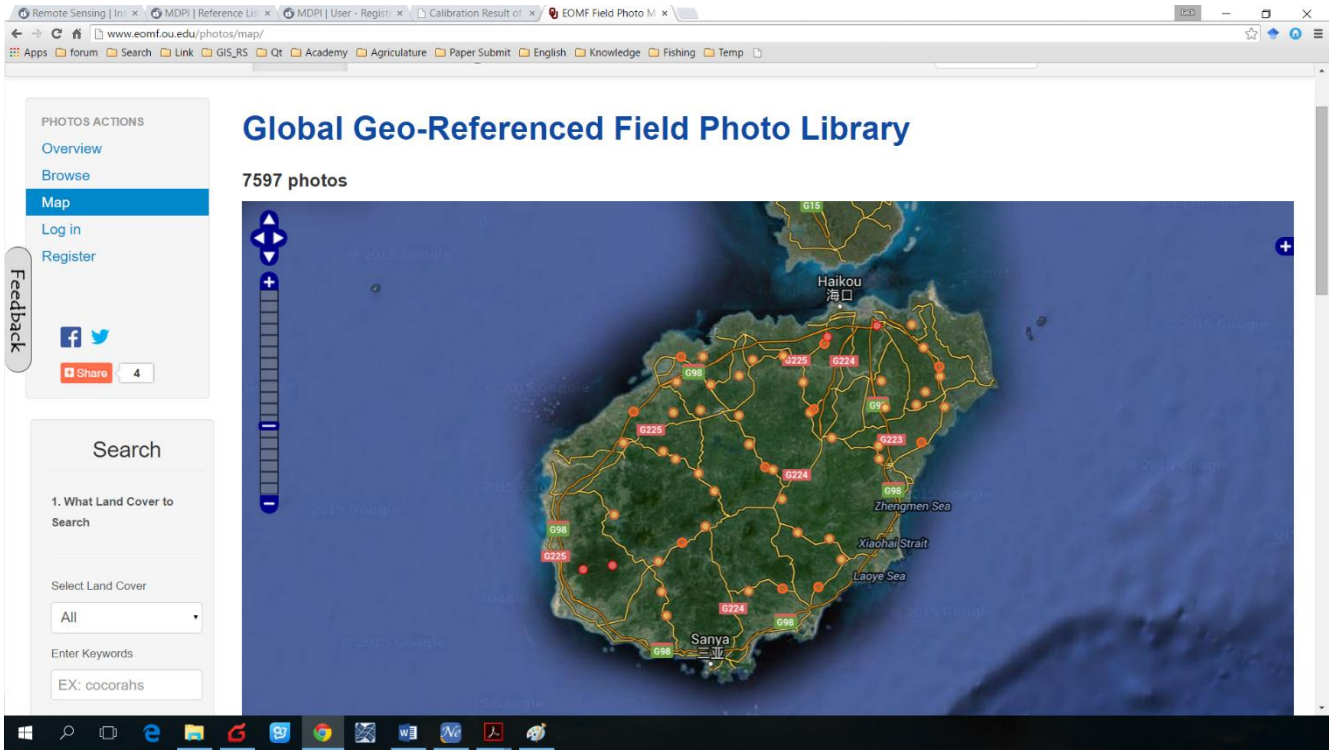

Fig. S1 Screenshot of Global Geo-Referenced Field Photo Library in Hainan Island. The small color circles on the island indicate the collection of field photos in close regions. It contains 7597 field photos on the island right now. (http://www.eomf.ou.edu/photos/).